

# Fermi Surface and Band Structure of BiPd from ARPES Studies

H. Lohani,<sup>1</sup> P. Mishra,<sup>1,\*</sup> B. R. Sekhar,<sup>1,†</sup> Anurag Gupta,<sup>2</sup> and V. P. S. Awana<sup>2</sup>

<sup>1</sup>*Institute of Physics, Sachivalaya Marg, Bhubaneswar- 751005, India.*

<sup>2</sup>*National Physical Laboratory(CSIR),*

*Dr. K. S. Krishnan Road, New Delhi 110012, India.*

(Dated: October 31, 2023)

We present a detailed electronic structure study of the non-centrosymmetric superconductor BiPd based on our angle resolved photoemission spectroscopy (ARPES) measurements and Density Functional Theory (DFT) based calculations. We observe a high intensity distribution on the Fermi surface (FS) of this compound resulting from various electron and hole like bands which are present in the vicinity of the Fermi energy ( $E_f$ ). The near  $E_f$  states are primarily composed of Bi-6p with a little admixture of Pd-4d<sub>x<sup>2</sup>-y<sup>2</sup>/z<sup>2</sup></sub> orbitals. There are various spin-orbit split bands involved in the crossing of  $E_f$  making a complex FS. The FS mainly consists of multi sheets of three dimensions which disfavor the nesting between different sheets of the FS. Our comprehensive study elucidates that BiPd is essentially a s-wave multiband superconductor.

PACS numbers: 74.25.Jb, 74.70.Dd, 71.20.Be

## I. INTRODUCTION

An upsurge has been witnessed recently in the search for novel materials after realizing the significant role of spin-orbit coupling (SOC) effects in the modification of near Fermi level ( $E_f$ ) electronic structure of materials and thereby their physical properties. For example, presence of a strong SOC produces conducting edge states in topological insulators (TIs)<sup>1,2</sup>. Similarly, intertwining of the spin-orbit interaction with non-centrosymmetric (NCS) structures gives rise to some exotic phenomena of mixing up of spin-singlet and triplet Cooper pairing channels<sup>3,4</sup> in superconductors (SCs). The anomalous value of upper critical field ( $H_{c2}$ )<sup>5,6</sup>, presence of Majorana surface states at the junction of superconducting transition temperature ( $T_c$ )<sup>7,8</sup> and existence of Weyl fermion surface states in Weyl semimetals<sup>9</sup> are a few more interesting properties related to the NCS structures behaving under SOC effects. These new class of materials not only present intriguing physics but also have tremendous scope in various applications.

One of the interesting aspects of the NCS crystals is a broken inversion symmetry that gives rise to antisymmetric spin-orbit interaction (ASOC) which has been theoretically predicted to form an unconventional pairing in the NCS SCs. However, most of the NCS SCs, like Mg<sub>10</sub>Ir<sub>19</sub>B<sub>16</sub><sup>10</sup>, Mo<sub>3</sub>Al<sub>2</sub>C<sup>11</sup>, Re<sub>24</sub>Nb<sub>5</sub><sup>12</sup>, Re<sub>3</sub>W<sup>13</sup> show conventional s-type superconducting behavior which is attributed to the weak SOC in these compounds. The pairing mechanism becomes quite complex due to strong electron correlation effects in some other SCs of the NCS family, like CePt<sub>3</sub>Si<sup>14</sup>, UIr<sup>15</sup>. In this scenario, discovery of superconductivity in NCS compound BiPd has brought some new excitement to this field due to the presence of heavy elements Bi ( $Z = 83$ ) and Pd ( $Z = 46$ ). SOC is expected to be strong while electronic correlation is moderate in this compound as suggested by Kadowaki-Woods value estimated from resistivity measurements<sup>16</sup>. Therefore, it provides an excellent ground to study the role of SOC effects in the electronic structure of NCS SCs. BiPd shows a transition from orthorhombic ( $\beta$ -BiPd) to monoclinic ( $\alpha$ -BiPd) structure at 210°C and its  $T_c$  is  $\sim 3.7$  K<sup>17,18</sup>. Vari-

ous measurements, like electrical resistivity, magnetic susceptibility and heat capacity helped in establishing a s-wave type BCS superconductivity in this system<sup>17,19</sup>. However, mixing of spin-singlet and triplet order parameter, signature of multi-gap and Andreev bound states have also been identified from Andreev spectroscopic measurements<sup>20</sup>. Spin-triplet component has also been seen in the nuclear quadrupole resonance (NQR) measurements<sup>21</sup>. Similarly, London penetration depth and its corresponding superfluid density showed an anisotropy with two energy gaps which was further attributed to the mixing of the two pairing states in BiPd<sup>22</sup>. But, so far, there is no consensus reached on the role of ASOC induced spin-triplet pairing in the formation of Cooper pairs. Further, another promising feature, a Dirac cone like surface state has been observed recently in angle resolved photoemission spectroscopy (ARPES) study by Hasen *et al.*<sup>23</sup>. This non-trivial topological character in the superconducting state may pave the path for experimental realization of Majorana states in this system.

Till date there is only one experimental photoemission study reported on BiPd<sup>23</sup> which is mainly focused on the surface state bands. In this report, our aim is to investigate the near  $E_f$  electronic structure of BiPd by using ARPES measurements and discuss these results in detail along with our calculations based on density functional theory (DFT). We observe a high intensity distribution on the Fermi surface (FS) resulting from various electron and hole like bands present in the vicinity of  $E_f$ . These near  $E_f$  states are composed primarily of Bi-6p with a little admixture of Pd-4d<sub>x<sup>2</sup>-y<sup>2</sup>/z<sup>2</sup></sub> orbitals. The FS mainly consists multi sheets of three dimensions (3D) which are due to several spin-orbit splitted bands crossing the  $E_f$ . This 3D character does not favor the nesting between the different sheets of FS and weakens the possibility of any density wave instabilities in this system. Our results emphasize that the pairing is essentially a spin-single nature mediated by the phonons in BiPd.

## II. EXPERIMENTAL AND CALCULATION DETAILS

A high quality single crystal of BiPd was synthesized via self flux melt growth technique. Stoichiometry was confirmed by using X-ray diffraction measurements. Results of the structural and other physical characterizations have been reported earlier<sup>16</sup>. Photoemission spectra were collected in angle resolved mode by using a hemispherical SCENTA-R3000 analyzer and a monochromatized He source (SCENTA-VUV5040). The photon flux was of the order of  $10^{16}$  photons/s/steradian with a beam spot of 2 mm in diameter. Fermi energy for all measurements were calibrated by using a freshly evaporated Ag film on to the sample holder. The total energy resolution, estimated from the width of the Fermi edge, was about 27 meV for the He-I excitation. Measurements were performed at a base pressure of  $\sim 2.0 \times 10^{-10}$  mbar at temperature 77 K. A fresh surface of the sample was prepared by *in-situ* cleaving using post-technique method in the preparation chamber at base pressure of  $5.0 \times 10^{-10}$  mbar and the spectra were taken within 4.0 hour, so as to avoid any surface degradation. All the measurements were repeated many times to ensure the reproducibility of the data.

First-principles calculations were performed by using a plain wave basis set inherent in Quantum Espresso(QE)<sup>24</sup>. Many electron exchange-correlation energy was approximated by Perdew-Burke-Ernzerhof (PBE) functional<sup>25-27</sup>. Both fully relativistic ultrasoft<sup>28</sup> and non relativistic norm-conserving pseudopotentials were used in the calculations in order to see the SOC effects. Fine mesh of k-points with Gaussian smearing of the order 0.0001 Ry was used for sampling the Brillouin zone integration, and kinetic energy and charge density cut-off were set to 100 Ry and 500 Ry respectively. Experimental lattice parameters and atomic coordinates of  $\alpha$ -BiPd<sup>18</sup>, after relaxed under damped (Beeman) dynamics with respect to both ionic coordinates and the lattice vector, were employed in the calculations. All parameters were optimized under several convergence tests.

## III. RESULT AND DISCUSSION

Fig.1(a) shows the crystal structure of  $\alpha$ -BiPd, in which Bi (Blue) and Pd (Red) atoms are arranged in two adjacent double layers. The bonding between alternative layers is weak which makes the (010) plane good for cleaving. Bi(Pd) atoms are coordinated to Pd(Bi) atoms situated at seven nearest neighbour (nn) sites as shown in Fig.1(b). The average inter-atomic distance of Pd atoms (1-4) from the Bi atom is 2.85 Å while the Pd atoms 5 and 6 are at 2.89 Å apart. Similarly, Pd atom 7 placed on the adjacent double layer is separated by 2.88 Å from the Bi atom. Fig.1(c) present the 2D surface Brillouin zone (BZ), where the high symmetry k-points  $\Gamma$ , X, Z and T are shown along with blue arrows indicating the k-directions along which we performed our calculations.

Fig.2(a) shows the ARPES intensity map of the FS of BiPd on the  $\Gamma$ -Z plane. It can be clearly seen from this plot that intensity distribution varies significantly at different k-points and it is substantially less around the  $\Gamma$  point. This distribu-

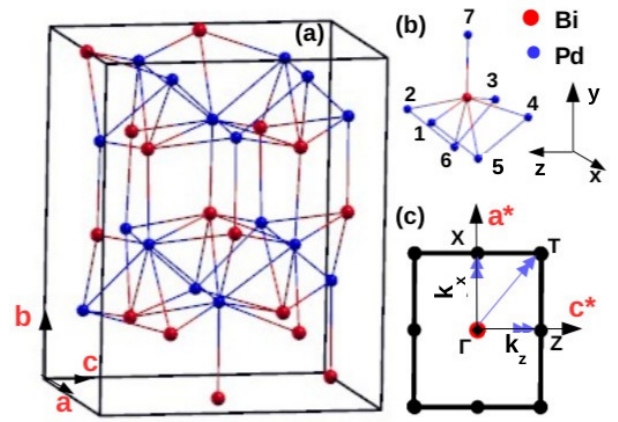


FIG. 1. (Color online)(a) Crystal structure of  $\alpha$ -BiPd. (b) The coordination environment of Bi(Pd). (c) The 2D surface Brillouin zone of BiPd where  $\Gamma$ , Z, X and T are the high symmetry k-points and blue arrows denote the k-direction of band mapping.

tion gradually increases as we move along the  $\Gamma$ -Z direction and quite high intensity is observed around the Z point. The images of energy dispersion along different cuts from #1 to #3 are displayed in Fig.2(b)-(d) respectively. In Fig.2(b), a high intensity region can be found at  $\sim E_b = -0.9$  eV and  $k_{||} = -0.32 \text{ \AA}^{-1}$  which rapidly disperses towards the higher binding energy as k approaches to the  $\Gamma$  point. Similarly, moderate intensity is observed near the  $E_f$  and around  $E_b = -0.6$  eV which also shows a strong dispersion. Intensity gets modified remarkably along the other two cut directions (#2 and #3). Here, intense patches of intensity distribution can be found, particularly around the center k point in the vicinity of  $E_f$  in comparison to cut #1. Likewise, high intensity regions are also observed in many parts on the  $\Gamma$ -T plane of the FS as shown in Fig.2(e). Again, the intensity distribution is quite low around the  $\Gamma$  point, whereas it is moderate around T point. Band dispersion along cut #4 to #7 is displayed in Fig.2(f)-(i) respectively. In Fig.2(f), two parabolically dispersing bands can be viewed in the higher BE region ( $E_b = -0.7$  to  $-1.1$  eV). Similarly, places of high intensity are also observed close to the  $E_f$  at  $\sim k = \pm 0.22 \text{ \AA}^{-1}$ . These intensity distributions evolve drastically on scanning the different cuts along the  $\Gamma$ -T direction. In the image of cut #5, bands are more intense in the BE range  $\sim E_b = -0.2$  to  $-0.6$  eV relative to cut #4 and again become less intense in the next images collected along the cut #6 and #7. The observed high intensity distribution at various parts of both the FS plots, which results from the different electronic bands, confirms the good metallic character of BiPd. This observation is also consistent with the resistivity behavior of BiPd<sup>17</sup>. Broadening of the bands which lead to intensity patches in the energy dispersion plots could be an outcome of the large number of closely spaced bands which are not well resolved in these ARPES images or the sizable contribution coming from interlayer 3D coupling<sup>29</sup>. Nevertheless, the strongly dispersive nature of different intensity patterns indicate a weakly correlated character of BiPd. In order to elucidate the nature of the near  $E_f$  states a compar-

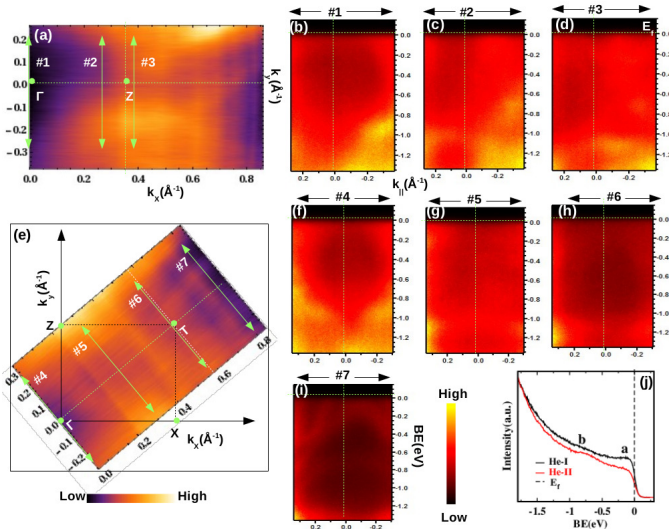


FIG. 2. (Color online)(a) and (e) ARPES intensity map of FS on  $\Gamma$ -Z and  $\Gamma$ -T plane respectively. (b)-(d) ARPES images of energy dispersion along different cuts #1 to #3 and (f)-(i) same images taken along cuts #4 to #7 respectively. (j) Comparison of angle integrated valence band spectra of BiPd collected at He-I(black) and He-II(red) photon energy.

ision of angle integrated valence band photoemission spectra are presented in Fig.2(j) taken at He-I (21.2 eV) and He-II (40.8 eV) photon energy respectively. In He-I spectra (Black), two features 'a' and 'b' are visible positioned close to the  $E_f$  and at  $\sim E_b = -0.9$  eV respectively. This near  $E_f$  feature (a) is suppressed in He-II spectra (Red) while the intensity of the higher BE feature (b) is slightly enhanced in comparison to the He-I case. These changes in the spectral weight signify that the near  $E_f$  bands (a) could be mainly composed of Bi-6p whereas Pd-4d contribution is dominant in the higher BE feature (b) (atomic photoionization crosssections<sup>30</sup> of Bi-6p and Pd-4d are different for He-I to He-II).

In order to get a deeper insight into the underlying physics behind the near  $E_f$  bands, an enlarged view of this region in the Fig.2(b) and (d) are shown in Fig.3(a) and (b) respectively. Similarly, Fig.3(c), (d) and (e) correspond to the near  $E_f$  zoomed images of the Fig.2(f), (h) and (i) respectively. In these plots large spectral weight can be seen which indicates the presence of various bands crossing the  $E_f$ . In order to resolve this crossings of near  $E_f$  bands more clearly, images Fig.3(a)-(e) are renormalized by dividing their angular integrated spectrum and presented in Fig.3(f)-(j) respectively. In Fig.3(f) three bands can be identified; two of them hole like ( $\alpha$  and  $\beta$ ) and one electron like ( $\gamma$ ). The apex of  $\alpha$  band lies  $\sim E_b = -0.25$  eV at the  $\Gamma$  point while the band  $\beta$  crosses the  $E_f$  at  $\sim k_{\parallel} = \pm 0.1 \text{ \AA}^{-1}$  and leads to a hole pocket around the  $\Gamma$  point. On the other hand, small traces of the electron like band  $\gamma$  is found at  $\sim k_{\parallel} = 0.3 \text{ \AA}^{-1}$  which probably forms an electron pocket around the X point. Similarly, intensity distribution in the vicinity of the Z point (Fig.3(g)) shows the presence of a one electron like band around the Z point and a hole like band touching the  $E_f$  nearby the Z point. Whereas, along the  $\Gamma$ -T

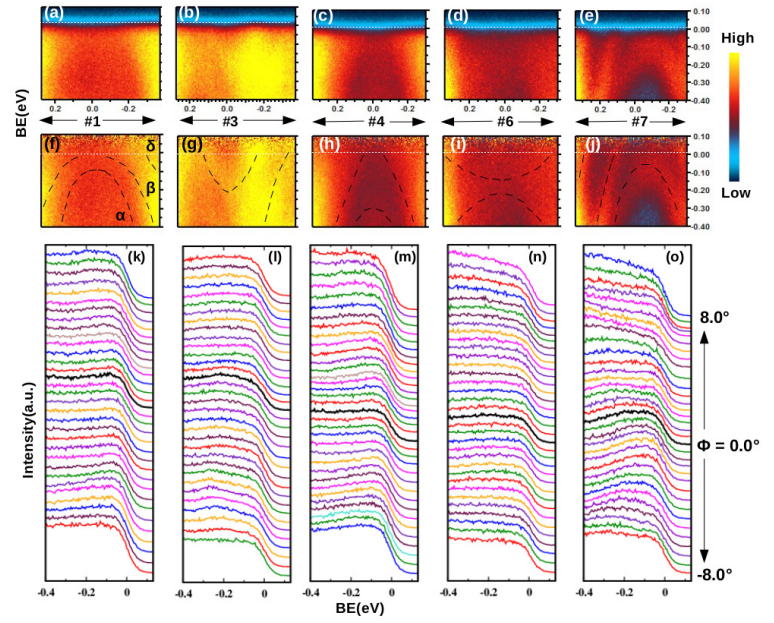


FIG. 3. (Color online)(a)-(e) show near  $E_f$  region of ARPES intensity plot along cut#1, #3, #4, #6 and #7 and corresponding renormalized images by angular integrated spectrum are shown in (f)-(j) respectively. In (k)-(o) energy density curves(EDC) extracted from (a)-(e) are displayed

direction two hole like bands ( $\alpha'$  and  $\beta'$ ), similar to the bands along the  $\Gamma$ -X direction are observed around the  $\Gamma$  point as clear from the Fig.3(h). The apex of one band ( $\beta'$ ) is at higher BE ( $E_b \sim -0.3$  eV) while the other band ( $\alpha'$ ), which shows nearly a linear dispersion curves a hole pocket around the  $\Gamma$  point. This intensity pattern changes as traversing along this  $\Gamma$ -T direction as clear from the Fig.3(i) and (j) which correspond to ARPES images taken along the cut #6 and #7 respectively. Though, intensity of bands are not prominent along the cut #6, three hole like bands could be clearly seen along the cut #7. Two of them form hole pockets and the other band just touches the  $E_f$ . The difference in the band dispersion are also evident in energy density curves (EDC) plots as shown in Fig.3(k)-(o) which are extracted from the ARPES images Fig.3(a)-(e) respectively. In these EDC plots, sufficient spectral weight is seen close to the  $E_f$  and its variation with respect to  $\phi$  differs along various cuts.

We also performed first principles calculations to better understand our ARPES findings. In Fig.4(a) non-relativistic band structure of BiPd is presented where four electron pockets (red, blue, green and magenta) and two hole pockets (orange and cyan) are found around the X and  $\Gamma$  points respectively. The dispersion of the near  $E_f$  bands are slightly modified along the  $\Gamma$ -T direction in comparison to the  $\Gamma$ -X direction, however, the number of electron and hole pockets remain same. On the other hand, along the  $\Gamma$ -Z direction, two almost degenerate (indigo and brown) hole like bands cross the  $E_f$  close to the Z point leading to small hole pockets around the Z point. Moreover, one tiny electron pocket can also be observed between the  $\Gamma$  and the Z point formed by the cyan band.



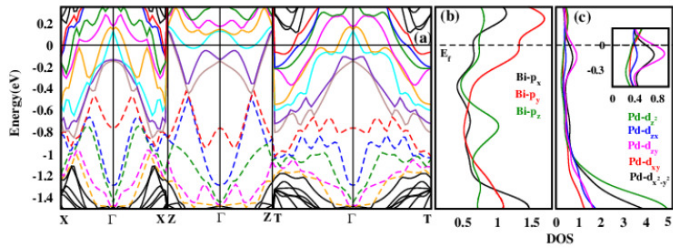


FIG. 4. (Color online) (a) Non relativistic band structure plot of BiPd. (b) and (c) DOS of individual B-6p and Pd-4d orbitals integrating from all the Bi and Pd atoms respectively.

These results are consistent to the resistivity measurements<sup>16</sup> predicting the moderate electronic correlation in BiPd by estimating Kadowaki-Woods value. To figure out the orbital character of these bands, orbital resolved DOS is calculated on the same k-space along which bands are obtained and smoothed by a Gaussian smearing. These results show that the DOS originate from Bi-6p and Pd-4d dominate the near  $E_f$  region and DOS of different 6p and 4d orbitals of individual Bi and Pd atoms are almost identical. So, in Fig.4(b) and (c) DOS of individual Bi-6p and Pd-4d orbitals integrating from all the Bi and Pd atoms are displayed. It can be clearly seen that Bi- $p_y$  contribution to the near  $E_f$  states is quite large in comparison to Bi- $p_{x/z}$  as well as sufficient weight of Pd- $d_{xy/x^2-y^2}$  (see the inset of Fig.4(c)) states are also present in this region. Comparing this plot to band picture, it is clear that the bands lying deeper in BE ( $E_b \sim -0.4$  to  $-1.0$  eV) red, blue and green (dashed line) and showing highly dispersive nature are mainly originated from different Bi-6p orbitals while bands  $E_b \sim -1.2$  eV (dashed magenta and orange) are mainly formed by Pd- $4d_{x^2-y^2/zy}$  orbitals. These results of band characteristics are consistent with the changes seen in the experimental spectral features 'a' and 'b' as moving from He-I to He-II excitation energy Fig.2(j). The electron pockets (red and blue) around the X point is dominated by Bi- $6p_x$  orbital while hole pockets (orange and cyan) around the  $\Gamma$  point are mainly composed of Bi- $6p_y$  orbital which is different from Bi- $6p_z$  character of hole pockets (indigo and brown) around the Z point. Similarly, the additional increment of Pd- $4d_{zy}$  and Pd- $4d_{zx}$  orbital character in the electron like bands around the T point is the possibly reason for modification of these bands in comparison to the same bands seen around the X point. These different nature of the near  $E_f$  bands, which are predominant by different Bi-6p orbitals could be associated to the coordination geometry of Bi atom as shown in Fig.1(b). It is clear that one of the lobe of Bi- $6p_y$  orbital is directed towards  $4d_{x^2-y^2}$  orbital of Pd atom (7) and the other side has proximity with  $4d_{yx}$  orbital of Pd (5 and 6). On the other hand, Pd atoms (1-4) form a geometry like a square planar coordination around the Bi atom which is tilted by  $30^\circ$  from the ZX plane. These arrangements and nearly equal inter-atomic distances of the Bi with these nn Pd atoms favor a strong intermixing between the different Bi-6p and Pd-4d orbitals and resulting bands span in the large energy range with varying contribution from the different orbitals.

To investigate the effects of SOC, band structure with in-

clusion of the SOC is calculated and illustrated in Fig.5(a). As clear from this plot that the various bands are splitted due to spin orbit interaction and the scale of splitting is varied at different k-points. Significant modification is observed in the bands which are placed in the vicinity of  $E_f$ . Several new electron and hole pockets with different sizes appear in comparison to the non SOC case (Fig.4(a)) Like, one hole pocket (orange band) between the  $\Gamma$  and X point, two electron pockets (green and brown band) between the  $\Gamma$  and Z point and electron pockets (maroon and yellow band) around the T point are the additional pockets. Moreover, the hole pocket shrinks remarkably around the Z point. These changes in the band structure signify that the SOC is quite pronounced and play an important role in constructing the FS topology in this system. There are many (18) spin-orbit split bands cross the  $E_f$  which give rise to a complex FS of BiPd as depicted in Fig.5(b). Shape of the FSs originating from different spin-orbit split bands is nearly identical. Mainly four types of distinct FS sheets can be identified which are shown in Fig.5(c), (d), (e), and (f) corresponding to the calculated band turquoise, indigo, blue and violet respectively. Two tiny electron pockets are visible at the center of zone faces in the FS made by turquoise band(5(c)) while two connected hole cones, one along  $k_z$  (larger in size) and second along  $k_y$  (smaller in size), are observed in the second FS sheet(5(d)). On the other hand, hole like FS sheet originated from the Bi- $6p_y$  (blue) dominated band(5(e)) extends along the  $k_y$  and  $k_z$  directions in a cylindrical tubular form. Similarly, the fourth FS sheet (5(f)) is composed of disconnected pieces of dumble shaped structure which are located at the edges of the BZ boundary. This type of FS comprising of several sheets of multidimensional character has also been witnessed in similar kind of SC BiPd<sub>2</sub><sup>31</sup> as well as some other NCS SCs Ca(Pt/Ir)Si<sub>3</sub><sup>32</sup>, LaPdSi<sub>3</sub><sup>33</sup> and Re<sub>24</sub>(Nb;Ti)<sub>5</sub><sup>34</sup>.

Comparing these results to ARPES findings, we find that the spectral weight distribution around the Z(Fig.5(e)) and T(Fig.5(f)) points in comparison to the  $\Gamma$  point which is consistent with the experimental FS plots where high intensity distribution is found around the Z and T points compared to the  $\Gamma$  point(Fig.??(a) and (e)). Likewise, in band structure along the  $\Gamma$ -X direction(Fig.5(a)) the blue bands meet the  $\Gamma$  point at  $E_b = -1.17$  eV and disperse strongly towards lower BE  $E_b = -0.6$  eV accompanied by the green bands. In the ARPES image Fig.??(b), intensity pattern shows the identical behaviour that is highly dispersive in the same BE range and crosses the Gamma point  $\sim E_b = -1.15$  eV. Further, the calculated red(dashed) band dispersion in the BE between  $E_b = -0.7$  eV to  $-0.48$  eV is similar to the intensity variation observed in the same BE range in ARPES data. The calculated bands lying in deeper BE(dashed green, blue, magenta) along the  $\Gamma$ -T(Fig.5(a)) direction show resemblance with the ARPES results(Fig.??(f)), like the  $\Gamma$ -X direction. However, in this image Fig.??(f) the change in the calculated red(dashed) band compared to the  $\Gamma$ -X direction is not identified. To consider the near  $E_f$  region, along the  $\Gamma$ -X direction the intensity pattern marked as an  $\beta$  band in (Fig.3(f)) appears to be the composite result of the calculated bands(violet, cyan), which form hole pockets around the  $\Gamma$  point and green,

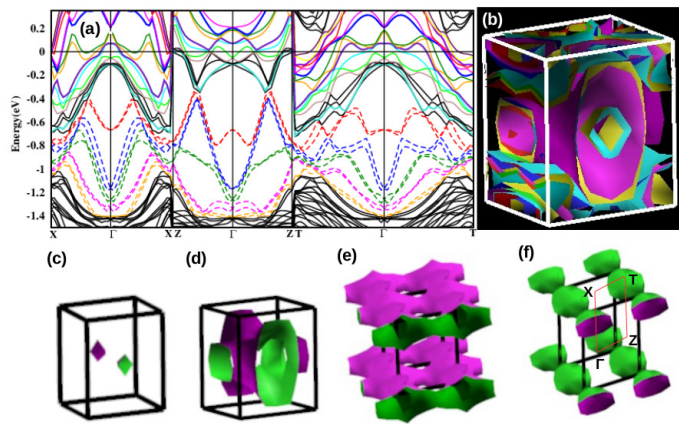


FIG. 5. (Color online) (a) Band structure plot of BiPd with including the SOC effects. (b) composite FS of BiPd. (c)-(f) Individual sheet of FS corresponding to calculated bands turquoise, indigo, blue and violet of (a) respectively.

brown(Fig.5(a)). Similarly, the dark green and orange electron like bands matches to the  $\delta$  band(Fig.3(f)) whereas the top of closely spaced cyan and black bands coincides with energy position of  $\alpha$  band in ARPES data(Fig.??(f)) after renormalized by a factor of 2.5. This value of renormalization is consistent with the resistivity measurements predicting the moderate electronic correlation in BiPd by estimating Kadowaki-Woods value<sup>16</sup>. Same scenario could also be seen along the  $\Gamma$ -T direction where composite structure of the calculated green, brown(Fig.5(a)) bands possibly leads to the  $\beta'$  band and renormalized cyan and black bands resulting the  $\alpha'$  structure in ARPES image(Fig.3(h)) taken along the  $\Gamma$ -T direction. Though, the bands are not clearly discernable in the ARPES data but composite intensity behaviour show a qualitative agreement with some of the calculated bands, particularly in the higher BE region. These results are helpful for further detailed electronic structure calculations in order to commensurate the DFT bands to ARPES results.

As it is clear from our band structure calculations and shown by our ARPES measurements (Fig.3(a)-(e)) various bands containing mainly Bi-6p with a little admixture of Pd-4d character are involved in the FS crossings. This highlights the possibility of multiband effects in this system, however, the strong 3D character of the different FS sheets weak-

ens the possibility of nesting between them and consequently existence of any density wave instabilities, like charge density wave (CDW) and spin density wave (SDW) are also less probable in this compound. Thus, the nature of Cooper pairing is expected to be more like spin-singlet assisted by phonons which has also been inferred previously from different experiments<sup>17,19</sup>. Interestingly, there are a few reports which explained these experimental observations in context of the coexisting spin-singlet and triplet pairing due to presence of ASOC in this compound<sup>20-22</sup>. Since, the ASOC split bands occur with different spin rotation because of interband SOC, the triplet pairing may be favored only at specific places in the resulting FS of such bands, like in other NC SC LaPtSi<sup>35</sup>. Hence its contribution could be quite less. Therefore, BiPd could be essentially a multiband s-wave SC.

#### IV. CONCLUSION

In our ARPES study of BiPd, we found that various bands are involved in the crossings of  $E_f$  along both the  $\Gamma$ -X and  $\Gamma$ -T directions. The FS depicts a high intensity distribution at various parts of the surface BZ which is consistent with the high metallic nature of BiPd. One hole pocket around the  $\Gamma$  point and an electron pockets around the X point are also identified from the near  $E_f$  ARPES intensity plots. These results show a fairly good agreement with the calculated band structure, mainly in the higher BE region, though the bands are not very discernable as predicted in the calculations. Our orbital resolved DOS calculation reveals that the near  $E_f$  states are primarily composed of Bi-6p orbitals with a little admixture of Pd-4d $_{x^2-y^2/zy}$  while the states at higher BE ( $\sim E_b = -1.2$  eV) are dominated by Pd-4d orbital character. This near  $E_f$  region is significantly modified with the inclusion of SOC effects and various new hole and electron pockets arising from the spin-orbit split bands appear in comparison to the non-relativistic case. FS manifested by these bands consists of multi sheets of different dimensions, mainly three dimensions which disfavor the nesting conditions and weakens the possibility for any density wave instabilities in this system. Since, spin split bands in AOSC driven systems have different spin rotation restricting the spin-triplet pairing at specific parts of the FS, like in NCS SC LaPtSi, the pairing should mainly be of singlet nature mediated via phonons.

\* Current address: Tata Institute of Fundamental Research, Homi Bhabha Road, Mumbai 400005, India

† sekhar@iopb.res.in

<sup>1</sup> M. Z. Hasan and C. L. Kane *Rev. Mod. Phys.* **82** (2010) 3045.

<sup>2</sup> Xiao-Liang Qi and Shou-Cheng Zhang *Rev. Mod. Phys.* **83** (2011) 1057.

<sup>3</sup> L. P. Gorkov and E. I. Rashba *Phys. Rev. Lett.* **87** (2001) 037004.

<sup>4</sup> P. A. Frigeri, D. F. Agterberg, A. Koga, and M. Sigrist *Phys. Rev. Lett.* **92** (2004) 097001.

<sup>5</sup> R. Jha, B. Tiwari, P. Rani, H. Kishan and V. P. S. Awana *J. Appl. Phys.* **115** (2014) 213903.

<sup>6</sup> Q. Zhang, G. Li, D. Rhodes, A. Kiswandhi, T. Besara, B. Zeng, J. Sun, Siegrist, M. D. Johannes and L. Balicas *Scientific Reports* **3** (2013) 1446.

<sup>7</sup> Liang Fu and C. L. Kane *Phys. Rev. Lett.* **100** (2008) 096407.

<sup>8</sup> David Hsieh, Y Xia, L Wray, Dong Qian, A Pal, JH Dil, J Osterwalder, F Meier, G Bihlmayer, CL Kane, YS Hor, RJ Cava, M Zahid Hasan *Science* **323** (2009) 919.

<sup>9</sup> Su-Yang Xu, Ilya Belopolski, Nasser Alidoust, Madhab Neupane, Guang Bian, Chenglong Zhang, Raman Sankar, Guoqing Chang, Zhujun Yuan, Chi-Cheng Lee, Shin-Ming Huang, Hao Zheng, Jie Ma, Daniel S. Sanchez, BaoKai Wang, Arun Bansil, Fangcheng

- Chou, Pavel P. Shibayev, Hsin Lin, Shuang Jia, M. Zahid Hasan *Science* **349** (2015) 613.
- <sup>10</sup> T. Klimczuk, F. Ronning, V. Sidorov, R. J. Cava, and J. D. Thompson *Phys. Rev. Lett.* **99** (2007) 257004.
  - <sup>11</sup> I. Bonalde, H. Kim, R. Prozorov, C. Rojas, P. Rogl, and E. Bauer *Phys. Rev. B* **84** (2011) 134506.
  - <sup>12</sup> C. S. Lue, T. H. Su, H. F. Liu, and Ben-Li Young *Phys. Rev. B* **84** (2011) 052509.
  - <sup>13</sup> Y. Huang, J. Yan, Y. Wang, L. Shan, Q. Luo, W. Wang and Hai-Hu Wen *Supercond. Sci. Technol.* **21** (2008) 075011.
  - <sup>14</sup> R. Onuki, A. Sumiyama, Y. Oda, T. Yasuda, R. Settai and Y. Onuki *J. Phys. Condens. Matter* **21** (2009) 075703.
  - <sup>15</sup> T. Akazawa, H. Hidaka, T. Fujiwara, T. C. Kobayashi, E. Yamamoto, Y. Haga, R. Settai, and Y. Onuki *J. Phys. Condens. Matter* **16** (2004) L29.
  - <sup>16</sup> Rajveer Jha, Reena Goyal, P. Neha, V. Maurya, A. Srivastava, Anurag Gupta, S. Patnaik and V. P. S. Awana *Sup. Sci. and Tech.* **26** (2016) 25008.
  - <sup>17</sup> Bhanu Joshi, A. Thamizhavel and S. Ramakrishnan, *Phys. Rev. B.* **84** (2011) 064518.
  - <sup>18</sup> Y. C. Bhatt and K. Schubert, *J. of Less Comm. Metals* **64** (1979) 17.
  - <sup>19</sup> Zhixiang Sun, Mostafa Enayat, Ana Maldonado, Calum Lithgow, Ed Yelland, Darren C. Peets, Alexander Yaresko, Andreas P. Schnyder and Peter Wahl *Nature Comm.* **6** (2015) 6633.
  - <sup>20</sup> Mintu Mondal, Bhanu Joshi, Sanjeev Kumar, Anand Kamlapure, Somesh Chandra Ganguli, Arumugam Thamizhavel, Sudhansu S Mandal, Srinivasan Ramakrishnan and Pratap Raychaudhuri *Phys. Rev. B.* **86** (2012) 094520.
  - <sup>21</sup> Kazuaki Matano, Satoki Maeda, Hiroki Sawaoka, Yuji Muro, Toshiro Takabatake, Bhanu Joshi, Srinivasan Ramakrishnan, Kenji Kawashima, Jun Akimitsu, Guo-qing Zheng *J. Phys. Soc. Jpn.* **82** (2013) 084711.
  - <sup>22</sup> L. Jiao, J. L. Zhang, Y. Chen, Z. F. Weng, Y. M. Shao, J. Y. Feng, X. Lu, B. Joshi, A. Thamizhavel, S. Ramakrishnan, and H. Q. Yuan *Phys. Rev. B* **89** (2014) 060507(R).
  - <sup>23</sup> Madhab Neupane, Nasser Alidoust, Su-Yang Xu, Ilya Belopolski, Daniel S. Sanchez, Tay-Rong Chang, Horng-Tay Jeng, Hsin Lin, Arun Bansil, Dariusz Kaczorowski, M. Zahid Hasan, and Tomasz Durakiewicz *arXiv:1505.03466v1*.
  - <sup>24</sup> Giannozzi P. et al. <http://www.quantum-espresso.org>.
  - <sup>25</sup> Perdew J P, Burke K and Ernzerhof M *Phys. Rev. Lett.* **77** (1996) 3865.
  - <sup>26</sup> Perdew J P and Wang y *Phys. Rev. B* **45** (1992) 13244.
  - <sup>27</sup> Perdew J P, Chevary J A, Vosko S H, Jackson K A, Pederson M R, Singh D J and Fiolhais C *Phys. Rev. B* **46** (1992) 6671.
  - <sup>28</sup> Vanderbilt D Soft self-consistent pseudopotential in a generalized eigenvalue formalism *Phys. Rev. B* **41** (1990) 7892.
  - <sup>29</sup> V. Brouet, W. L. Yang, X. J. Zhou, Z. Hussain, R. G. Moore, R. He, D. H. Lu, Z. X. Shen, J. Laverock, S. B. Dugdale, N. Ru and I. R. Fisher *Phys. Rev. B* **77** (2008) 235104.
  - <sup>30</sup> J.J. Yeh and I. Lindau *Atomic Data and Nuclear Data Tables* **32** (1985) 1-155.
  - <sup>31</sup> I. R. Shein and A. L. Ivanovskii *J. Supercond. and Nov. Magn.* **26** (2013) 1.
  - <sup>32</sup> V. V. Bannikov, I. R. Shein and A. L. Ivanovskii *ZhETF* **92** (2010) 381.
  - <sup>33</sup> M.J. Winiarski and M. Samsel-Czekala *Intermetallics.* **56** (2015) 44.
  - <sup>34</sup> M.J. Winiarski *J. Alloy and Comp.* **616** (2014) 1.
  - <sup>35</sup> Kneidinger, F., Michor, H., Sidorenko, A., Bauer, E., Zeiringer, I., Rogl, P., Blaas-Schenner, C., Reith, D., Podloucky, R. *Phys. Rev. B* **88** (2013) 104508.